CRYSTAL GROWTH & DESIGN

pubs.acs.org/crystal

Article

Control of Calcium Carbonate Crystallization in an Orthogonal Diffusion System

Yu Seob Shin,[⊥] Gábor Holló,[⊥] István Lagzi,* and Sung Ho Yang*

Cite This: *Cryst. Growth Des.* 2024, 24, 9994−10002

Read Online

ACCESS | Metrics & More | Article Recommendations

ABSTRACT: Crystallization in living organisms is highly regulated by both passive diffusion and active transport across the cellular membrane or plasm. There have been studies that mimic slow diffusion in a biological system to control crystallization using microfluidic devices and diffusion-limiting media. This study introduced an orthogonal diffusion system in which the outer calcium and carbonate ions were perpendicularly diffused into a hydrogel. This orthogonal setup opens up a new possibility in designing and engineering crystalline materials than traditional techniques utilizing collinear orthogonal diffusion fluxes of the reagents. Various microenvironments could be formed two-dimensionally in a hydrogel according to the ion flux and calcium to carbonate ratio in an orthogonal diffusion system. Through this, it was possible to systematically investigate the effect of different levels of ion flux and ratio on crystallization. Different ion fluxes and ratios resulted in different morphologies of calcium carbonate, such as otoconia-, rhombohedron-, rosette-, and sphere-shaped calcites. In addition, the crystallization process is supported by a numerical simulation.

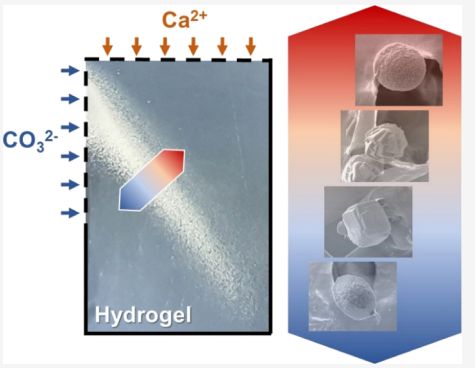

INTRODUCTION

In a biological system, a biomineral is controlled by the orchestration of soluble macromolecules and an insoluble matrix, resulting in hierarchical and functional structures. Many researchers intensively studied to understand biomineralization for the synthesis of new biomimetic materials.[1,2] However, it was focused on controlling the concentration of constituent ions and the supersaturation of solution to control the polymorphism and morphology of crystals.[3,4] In contrast, controlling the diffusion of ions has been less emphasized in previous studies on biomineralization. Mineralization in living organisms is highly regulated by both passive diffusion and active transport across the cellular membrane or plasm. For instance, during the calcification process in marine organisms, a liquid precursor composed of Ca^{2+}, HCO_3^-, and organics is transferred to calicoblastic cells by endocytosis and simultaneously transformed to hydrated amorphous calcium carbonate (ACC) form. Then, it is attached to the growing front of the calcification skeleton by exocytosis.[5] In addition, the bone and tooth formation mechanism in mammals is reported to be that dense calcium phosphate granules and calcium ions, which are generated in mitochondria, transport to the extracellular matrix (ECM) through intracellular vesicles, resulting in crystalline apatite.[6]

There have been studies that mimic slow diffusion in a biological system to control crystallization using microfluidic devices and diffusion-limiting media.[7,8] The microfluidic method has an advantage in that the mixing ratio of reactants can be precisely controlled in micrometer units. Still, it differs from the living organism conditions in which mass diffusion is slowly controlled through the cell membrane and plasm. In contrast with microfluidic devices, hydrogel as a diffusion-limiting medium has more similar conditions to living organisms,[9−15] because mass transfer in hydrogel media is slow and controlled by a restricted gel network. There have been studies that synthesize the various biominerals by controlling the nucleation and growth processes under slow diffusion conditions similar to those of living organisms.[16,17] Estroff et al. reported several fundamental effects that could control complex mineral structure through calcium carbonate crystallization studies in the hydrogel.[18] In particular, the hydrogel network provides the diffusion-controlled conditions necessary to achieve a wide range of shapes and structures of minerals. We previously found that three different morphologies of calcite (hopper, rosette, and otoconia) were systematically formed in an agarose hydrogel where the flux of external carbonate ions diffused into the agarose hydrogel acted as a significant factor controlling the crystal morphology.[15]

Received: August 19, 2024
Revised: November 5, 2024
Accepted: November 5, 2024
Published: November 19, 2024

On the other hand, stoichiometry on the activity of Ca^{2+} and CO_3^{2-} has been considered a significant factor for precipitation kinetics at the saturation state.[19−21] Growth and dissolution of calcium carbonate are affected by the anion-to-cation concentration ratio in aqueous solution because nonstoichiometric activities of Ca^{2+} and CO_3^{2-} are the general condition of most natural waters.[22−26] One of the studies reported a calcite morphology transition from regular rhombohedral to irregular rhombohedral and nanoparticle aggregations according to the CO_3^{2-}/Ca^{2+} ratio using microfluidic techniques for controlling the microenvironment of crystallization.[27] In addition, the effect of stoichiometry on the new formation and subsequent growth of $CaCO_3$ was investigated over a large range of solution stoichiometries ($10^{-4} < r_{aq} < 10^4$, where $r_{aq} = [Ca^{2+}]/[CO_3^{2-}]$).[28] This study shows that $[Ca^{2+}]/[CO_3^{2-}]$ in the solution strongly impacts the pathway and timing of $CaCO_3$ nucleation and growth. Many studies have been reported to explain the various effects of Ca^{2+} and CO_3^{2-} ratios on calcium carbonate crystallization.[27,29,30]

Despite the efforts of many studies, the effect of molar ratio on crystallization has not yet been clearly identified.[31] In addition, there are still limitations with respect to the bioinspired approach because most studies were investigated in experiment design based on the free solution. In the solution, various stoichiometric ratios can be easily controlled by adjusting the initial concentrations of reactants. However, the diffusion rate is high in such free media. Therefore, studying the elaborate effect of the stoichiometric ratio controlled by slow diffusion is challenging because reactants form products as soon as they encounter each other. To complement the limitation of experimental design based on solution, the hydrogel is an effective medium to simultaneously achieve slow diffusion and nonstoichiometric conditions. Therefore, it is possible to systematically study the effect of the stoichiometric ratio gradually changing in space and time from the initial stage to the final stage of the crystallization process.

This study introduced an orthogonal diffusion system in which outer Ca^{2+} and CO_3^{2-} ions were perpendicularly diffused into a hydrogel. This orthogonal setup opens up a new possibility in designing and engineering crystalline materials than traditional techniques utilizing collinear orthogonal diffusion fluxes of the reagents.[32−36] Agarose was chosen as a hydrogel medium because it has neutral hydroxyl groups, which are known to have relatively weak interactions with calcium carbonate.[37] Various microenvironments could be formed two-dimensionally in a hydrogel according to the ion flux and Ca^{2+}/CO_3^{2-} ratio in an orthogonal diffusion system. Through this, it was possible to systematically investigate the effect of different levels of ion flux and ratio on crystallization. We found that different ion fluxes and ratios resulted in different morphologies of calcium carbonate, such as otoconia-, rhombohedron-, rosette-, and sphere-shaped calcites.

EXPERIMENTAL SECTION

Materials. Calcium chloride dihydrate ($CaCl_2{\cdot}2H_2O$, BioReagent, ≥99.0%, Sigma-Aldrich), sodium carbonate decahydrate ($Na_2CO_3{\cdot}10H_2O$, puriss. p.a., ≥99.0%, Sigma-Aldrich), and agarose powder (Bacto-Agar, guaranteed grade, Becton-Dickinson) were used as they were purchased. Ultrapure water (18.3 MΩ·cm) from Human Power II+ (Human Science, Korea) was used for all solutions involved in the $CaCO_3$ crystallization.

Orthogonal Diffusion Crystallization of $CaCO_3$. A set of orthogonal diffusion crystallizations of $CaCO_3$ was performed in a slotted plastic tube filled with a 1% (w/v) agarose hydrogel (7 mL) at room temperature for 24 h. Seven mL of a 0.2 M $CaCl_2$ solution was poured on the hydrogel for the calcium ions to be diffused into the hydrogel in a vertical direction. At the same time, carbonate ions were diffused horizontally into the hydrogel by immersing the reaction tube in 25 mL of a 0.2 M Na_2CO_3 solution. The $CaCO_3$ crystals result from the orthogonal diffusion of Ca^{2+} and CO_3^{2-} into the agarose hydrogel. After the reaction, the samples were immersed in ultrapure water to remove the remaining electrolytes. The samples were freeze-dried for further characterization.

Characterization. The samples were completely dehydrated by a freeze-dryer (TFD8503, IlShinBioBase, Korea). For $CaCO_3$ crystal morphology observation, a scanning electron microscope (EVO LS10, Carl Zeiss, Germany) was used at a voltage of 5 kV. The samples were coated with Au using an ion sputtering instrument (Ion Sputtering Coater, KYKY-SBC-12, KYKY Technology Development Ltd., China). Energy-dispersive X-ray spectroscopy (EDS, Bruker, USA) was used to identify the atomic composition of precipitates. Crystal phases of $CaCO_3$ were measured using an X-ray diffractometer (JP/SmartLab, Rigaku Co. Ltd., Japan) equipped with Cu Kα1 radiation (λ = 1.540593 Å). The X-ray diffraction (XRD) data were collected from 20 to 60° angles with a step size of 0.02°. The pH was measured using a microelectrode (SevenCompact pH meter S220, Mettler Toledo Ltd., Switzerland).

Numerical Simulation. The precipitation model consists of the following chemical reactions, rate constants, and rates.

$$Ca^{2+} + CO_3^{2-} \rightleftharpoons C,\ k_1 = 10^{-2}\ M^{-1}\ s^{-1} \text{ and } k_{-1} = 10^{-5}\ s^{-1},\quad v_1 = k_1[Ca^{2+}][CO_3^{2-}],\ v_{-1} = k_{-1}[C] \tag{1}$$

$$C + C \rightarrow 2D,\ k_2,\ v_2 = k_2 \mathrm{Hill}([Ca^{2+}], [CO_3^{2-}])[C]^2 \tag{2}$$

$$C + D \rightarrow 2D,\ k_3,\ v_3 = k_3 \mathrm{Hill}([Ca^{2+}], [CO_3^{2-}])[C][D] \tag{3}$$

$$Ca^{2+} + CO_3^{2-} + D \rightarrow 2D,\ k_4 = 10^{-3}\ M^{-2}\ s^{-1},\quad v_4 = k_4[Ca^{2+}][CO_3^{2-}][D] \tag{4}$$

Here, C and D are the intermediate species ($CaCO_3$ nanoparticles) and precipitate ($CaCO_3$), respectively. The initial step in the precipitation model is the reversible formation of the intermediate from the reagents (eq 1). The intermediates aggregated with each other. They are subsequently transformed into crystalline precipitates described in eq 2. Once the precipitate is generated, it can grow by absorbing intermediates or constituent ions, as shown in eqs 3 and 4. The reaction rate coefficients for the reactions (eqs 2 and 3) were implemented by using the Hill function ($k_2 = k_3 = 10^{-1}/(1 + (([CO_3^{2-}] - [Ca^{2+}])/0.005)^2)\ M^{-1}\ s^{-1}$). If the concentrations of Ca^{2+} and CO_3^{2-} are identical, then the reaction rate coefficient is the greatest. However, if the excess of either Ca^{2+} or CO_3^{2-} increases, then the value of the function goes to zero, reflecting the fact that the excess of one of the ions can inhibit the precipitation due to the electrostatic stabilization of the formed nanoparticles. This precipitation model was coupled to the following equilibria

$$HCO_3^- \rightleftharpoons H^+ + CO_3^{2-},\ K_1 = 10^{-10.3} \tag{5}$$

$$H_2CO_3 \rightleftharpoons H^+ + HCO_3^-,\ K_2 = 10^{-6.4} \tag{6}$$

$$H_2O \rightleftharpoons H^+ + OH^-,\ K_w = 10^{-14} \tag{7}$$

The reaction-diffusion model, which describes the precipitation of $CaCO_3$, consists of a set of partial differential equations (PDEs) and identifies 8 chemical species

$$\partial_t c_i = D_i \nabla^2 c_i + r_i \tag{8}$$

where c_i, D_i, and r_i are the concentrations, diffusion coefficients, and kinetic terms of the corresponding chemical species, respectively, and

https://doi.org/10.1021/acs.cgd.4c01159
Cryst. Growth Des. 2024, 24, 9994−10002

∇ is the Nabla operator. The reaction-diffusion system (eq 8) was solved numerically using the method of lines technique: spatial discretization of the PDEs on an equidistant 2D grid with the size of 15 mm × 15 mm combined with a forward Euler method for the integration in time. The total time of the simulations was 1×10^5 s. We applied the following initial conditions in the computational domain (gel): $c_{Ca^{2+}}(t = 0,x,y) = 0$, $c_{CO_3^{2-}}(t = 0, x, y) = 0$, $c_{HCO_3^-}(t = 0, x, y) = 10^{-3}$ M, $c_{H_2CO_3}(t = 0, x, y) = 10^{-3}$ M, $c_C(t = 0,x,y) = 0$, $c_D(t = 0,x,y) = 0$, and $c_{H^+}(t = 0,x,y) = c_{OH^-}(t = 0,x,y) = 10^{-7}$ M; carbonate reservoir (Ω_1, $x = 0$, $y \in (0, 3$ mm$)$): $c_{Ca^{2+}}(t = 0,x,y) = 0$, $c_{CO_3^{2-}}(t = 0, x, y) = 1.6 \times 10^{-1}$ M, $c_{HCO_3^-}(t = 0, x, y) = 4 \times 10^{-2}$ M, $c_{H_2CO_3}(t = 0, x, y) = 0$, $c_C(t = 0,x,y) = 0$, $c_D(t = 0,x,y) = 0$, and $c_{H^+}(t = 0,x,y) = c_{OH^-}(t = 0,x,y) = 10^{-7}$ M; Ca^{2+} reservoir,(Ω_2, $x \in (0, 3$ mm$)$, $y = 0$): $c_{Ca^{2+}}(t = 0,x,y) = 2 \times 10^{-1}$ M, $c_{CO_3^{2-}}(t = 0, x, y) = 0$, $c_{HCO_3^-}(t = 0, x, y) = 10^{-3}$ M, $c_{H_2CO_3}(t = 0, x, y) = 10^{-3}$ M, $c_C(t = 0,x,y) = 0$, $c_D(t = 0,x,y) = 0$, and $c_{H^+}(t = 0,x,y) = c_{OH^-}(t = 0,x,y) = 10^{-7}$ M. We applied no-flux boundary conditions for all chemical species except for domains Ω_1 and Ω_2, where the Dirichlet boundary conditions (fixed concentrations at the boundary) were applied. The concentrations were applied based on the initial conditions and equilibrium reactions (eqs 5−7). The diffusion coefficient of Ca^{2+}, CO_3^{2-}, HCO_3^-, and H_2CO_3 was 10^{-9} m^2 s^{-1}, and H^+ and OH^- had a diffusion coefficient of 9.3×10^{-9} m^2 s^{-1}. The formed nanoparticles (C) and the precipitate could not diffuse. We used 1.5×10^{-1} mm and 1 s for the grid spacing and time step, respectively.

RESULTS

In an orthogonal diffusion system, Ca^{2+} and CO_3^{2-} ions diffused perpendicularly into an agarose hydrogel, and crystallization occurred along the diagonal position (Figure 1a). Various microenvironments differing by the concentration and the ratio of Ca^{2+} and CO_3^{2-} are spatiotemporally displayed in the hydrogel. Although the diffusion rate of Ca^{2+} and CO_3^{2-} is different, the diagonal position is supersaturated because the 1:1 stoichiometric ratio of Ca^{2+} and CO_3^{2-} is mostly satisfied at a similar distance from each reservoir. It was found by scanning electron microscopy (SEM) analysis that four types of dominant shapes were formed after 24 h, and those are named otoconia, rhombohedron, rosette, and sphere (Figure 1b−f). Each shape was distributed in the order of otoconia (blue), rhombohedron (green), rosette (yellow), and sphere (orange) near the CO_3^{2-} reservoir, and their average sizes were approximately 36, 52, 52, and 22 μm, respectively. In other words, the otoconia mainly formed at the closest to the CO_3^{2-} reservoir, while the sphere did at the closest to the Ca^{2+} reservoir. To examine the effect of the concentration of Ca^{2+} and CO_3^{2-}, the concentrations of both reservoirs were altered to 0.1, 0.25, and 0.5 M, and then crystallization was conducted. However, the shapes of the crystals and their distributions were almost identical regardless of the concentration of Ca^{2+} and CO_3^{2-} in the reservoirs.

The position of the turbid front was recorded for 24 h during crystallization (Figure 2a). The front rapidly travels in an initial stage, but it slows down over time. The crystallization was retarded at the farther position from the reservoir because of the diminished flux of ions. Because the flux of outer ions is related to the distance from their reservoir, the hydrogel was divided into three regions (I, II, and III) according to the slope of the graph. To understand the effect of ion flux on crystallization, the number density and average size of crystals were measured at each region. The density of formed crystals gradually decreased in the order of regions I, II, and III from

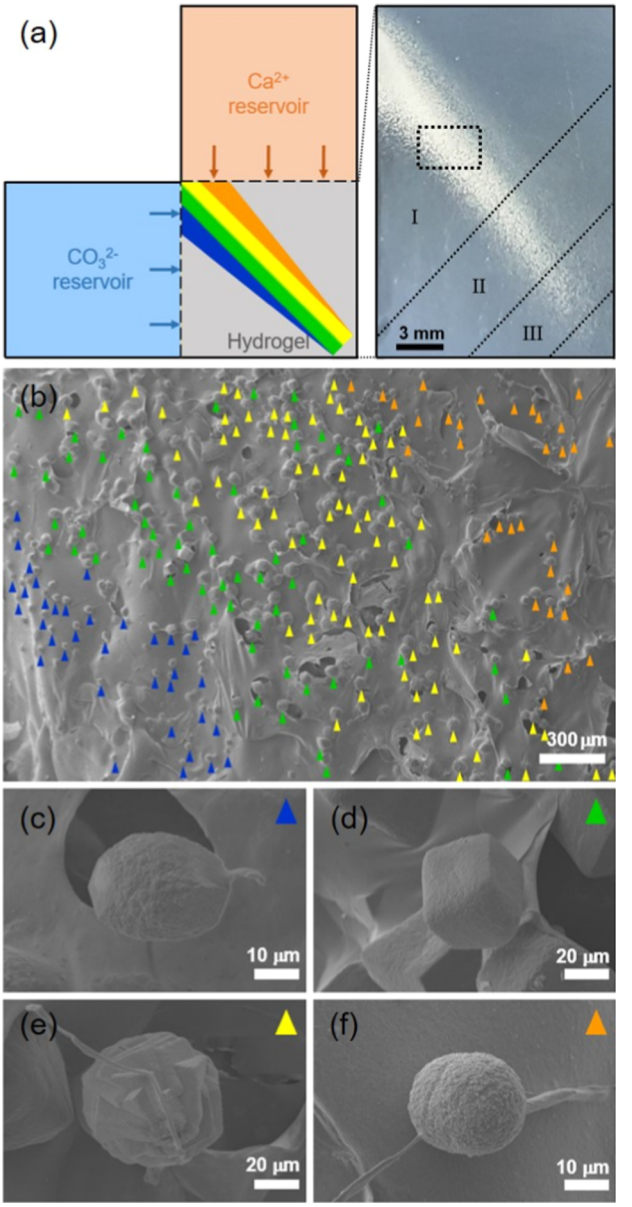

Figure 1. (a) Scheme (left) and optical image (right) of the orthogonal diffusion system for $CaCO_3$ crystallization in a hydrogel; (b) SEM micrograph of $CaCO_3$ crystals formed with 0.2 M $CaCl_2$ and 0.2 M Na_2CO_3 after 24 h, in a dotted box in (a); and magnified micrographs of (c) otoconia (blue), (d) rhombohedron (green), (e) rosette (yellow), and (f) sphere (orange).

31.4, 20.1, to 16.3 in a millimeter square, respectively (Figure 2b). 72% of total crystals formed in region I, but only 8% formed in region III. The crystallization was promoted at the closer position from the reservoir, while it retarded at the farther position from the reservoir. Four types of shapes were observed in all regions, but the average size of otoconia, rhombohedron, and rosette decreased in the order of regions I, II, and III (Figure 2c). Exceptionally, the sphere size was nearly the same regardless of the region. The distribution ratio of each shape was altered in each region (Figure 2d). If the sphere portion was excluded, the ratio of otoconia and rosette increased, while that of rhombohedron decreased in the order of regions I, II, and III. This result is consistent with our previous report conducted in a single diffusion system; the shape of crystals was altered by distance from the ion reservoir,

https://doi.org/10.1021/acs.cgd.4c01159
Cryst. Growth Des. 2024, 24, 9994−10002

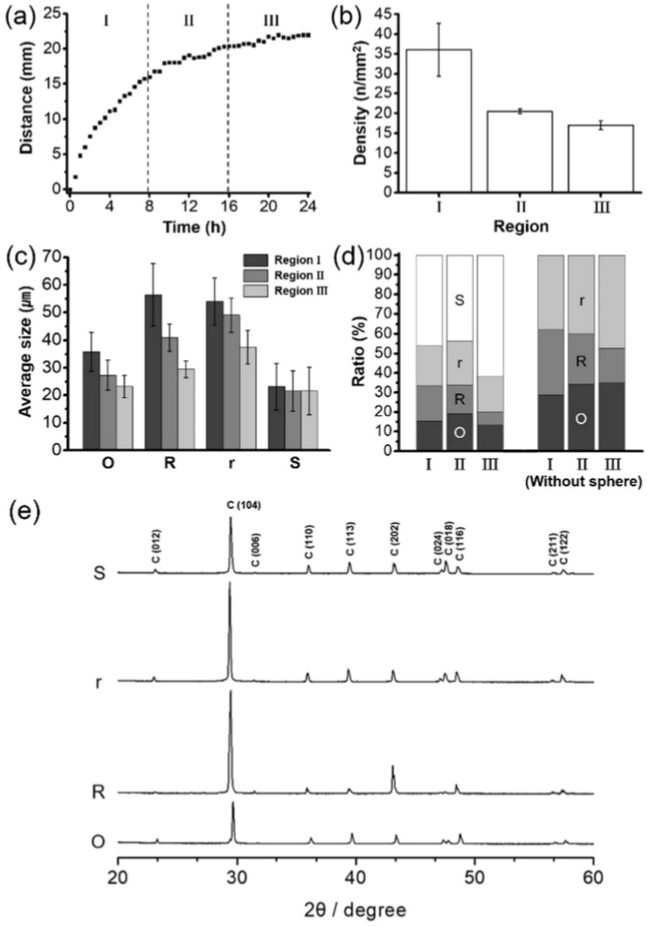

Figure 2. (a) Propagation of the turbid front as a function of time, and the hydrogel was divided into 3 regions (I, II, and III). (b) Number density of $CaCO_3$ crystals at each region. (c) Average size of each $CaCO_3$ crystal. (d) Ratio of crystal distribution by morphology at each region (O: otoconia, R: rhombohedron, r: rosette, and S: sphere). (e) XRD spectra of each crystal by shape.

which effects the intensity of ion flux.[15] Collectively, the number density, size, and distribution of crystals were altered by ion fluxes of both Ca^{2+} and CO_3^{2-}. The alteration can be explained by different levels of supersaturation in each region because the supersaturation level of each region is regulated by the ion flux in our system. XRD confirmed that a crystal phase of all $CaCO_3$ was calcite, regardless of their shape (Figure 2e). The peak assigned to the (104) face of calcite was the strongest in common at 29.4°, and the other characteristic (012), (110), (113), and (202) peaks were consistently observed at 23.2, 36.1, 39.6, and 43.4° from all spectra. However, the intensity of the (202) peak from the rhombohedron was relatively stronger than those of the others. The XRD data indicate that the crystals are transformed to a thermodynamically stable phase, although the initial phase differed. In addition, the crystallinity of each region was analyzed by XRD (not shown). The phase of crystals was calcite in all regions, and the intensity of the peaks was relatively weaker in region III than in regions I and II because of the low number density of crystals. Although the number density and size of crystals were affected by the intensity of ion flux, it is noteworthy that four shapes of crystals were observed in an entire region.

To elucidate different shapes of crystals in a hydrogel, we investigated various factors that possibly control the $CaCO_3$ morphology. Since directly measuring ion concentration in a hydrogel is technically difficult, pH measurement can be an alternative tool for estimating the supersaturation level because carbonate anion raises the pH. The pH of the reaction front in regions I, II, and III was measured as a function of time at three positions (Figure 3a), which were divided into the near carbonate reservoir (near Cb: blue in Figure 1a), middle (Mid: green and yellow in Figure 1a), and near calcium reservoir (near Ca: orange in Figure 1a). The pH was different at each position: 10−11, 9−10, and 8−9 at near Cb, Mid, and near Ca, although the pH of each position was almost the same regardless of regions and time. On the other hand, the pH decreased in the order of position near Cb, Mid, and near Ca. The difference in pH is matched by the distribution of different crystal shapes (Figure 1b). The pH of the position decreased in the order of otoconia, rhombohedron, rosette, and sphere (Figure 3b). In other words, otoconia formed at the highest pH, and spheres formed at the lowest pH, regardless of region.

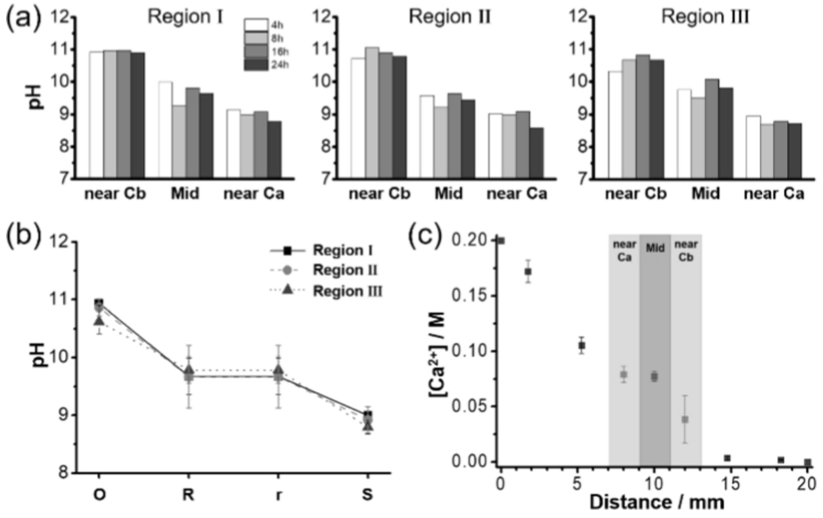

Figure 3. (a) pH of the hydrogel at different positions and times. (b) pH graph showing the relationship between pH and morphology (O: otoconia, R: rhombohedron, r: rosette, and S: sphere). (c) Ca^{2+} concentration along the distance from the Ca^{2+} reservoir.

https://doi.org/10.1021/acs.cgd.4c01159
Cryst. Growth Des. 2024, 24, 9994−10002

Noticeably, the initial pH of each position was maintained during the crystallization process. The pH after 24 h was similar to that after 4 h at each position. It implies that the initial conditions of stoichiometry and the supersaturation level determined the shape of the crystal. The calcium ion concentration ($[Ca^{2+}]$) was measured using a calcium ion-selective electrode after separating and dissolving the part of a hydrogel in distilled water. The calcium concentration gradually decreased as a function of the distance from the calcium reservoir (Figure 3c). By combining the measured Ca^{2+} concentration and the ratio of $[CO_3^{2-}]/[HCO_3^-]$ estimated from the pH value, the relation between the final shape of the crystal and the ratio of calcium and carbonate ions can be inferred. The calcium and carbonate ion activity ratio significantly deviated from the stoichiometric value at near Ca and indicated the carbonate limit-crystallization conditions. At Mid, the ratio of calcium and carbonate ion activities mostly satisfied the stoichiometric value close to 1:1. At near Cb, the ratio of calcium and carbonate ion activities significantly deviated from the stoichiometric value similar to near Ca and indicated the calcium-limited crystallization conditions.

The different shapes of each crystal were microscopically analyzed with SEM and EDS (Figure 4). With respect to surface textures, otoconia and rhombohedrons have a similar feature, which was covered with (104) facets and partially developed (*hk*0) facets (Figure 4a,b). The (104) faces were smoother, but the (*hk*0) surface was rougher. The different texture is mainly caused by the degree of the order in stacking the facets. A single layer of (104) faces formed orderly, but an inconsistent stack of layers formed the rough surface of the side.[15] In a magnified image, it was observed that more hydrogel fibers were incorporated in a rough (*hk*0) facet than in a smooth (104) facet. On the other hand, the surface texture of the rosette and sphere was rough and composed of agglomerated small particles (Figure 4c,d). Many fibers were incorporated between the agglomerated particles. In appearance, they gradually changed from single crystal to polycrystalline to amorphous solids in the order of otoconia, rhombohedron, rosette, and sphere. To confirm the relative amount of the incorporated hydrogel on each surface, the C/Ca ratio was measured by EDS (Figure 4e). In the cases of otoconia and rhombohedron, the C/Ca ratio of the rough facet is higher than that of the smooth (104) facet, which indicates that the hydrogel is more incorporated into the rough facet. It could be inferred that otoconia and rhombohedra were anisotropically formed by selective incorporation of the hydrogel on each facet. In the rosette and sphere cases, the ratio was not distinguishable on any surface, meaning that the hydrogel was uniformly incorporated into the crystal surface. It could be inferred that the rosette and sphere were isotropically formed with a uniformly incorporated hydrogel.

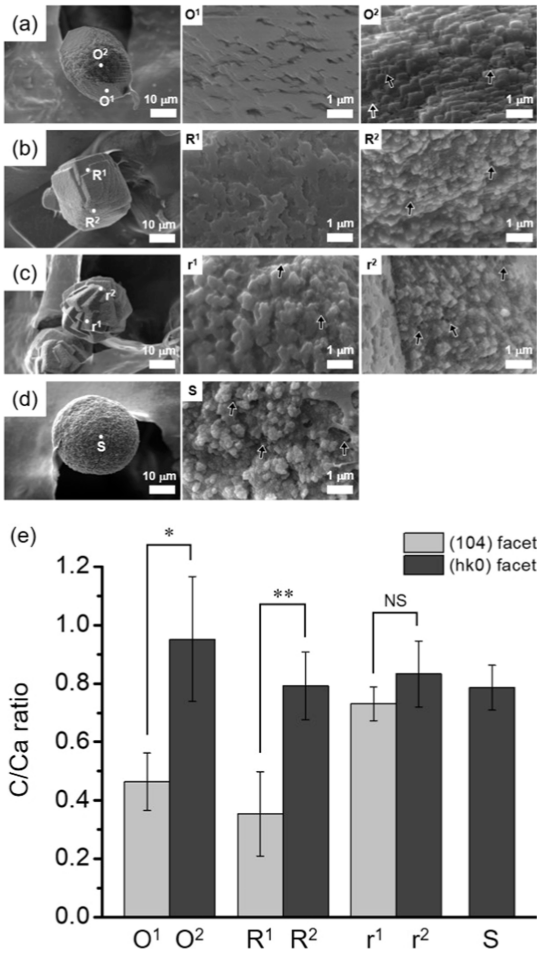

Figure 4. SEM micrographs of (a) otoconia, (b) rhombohedron, (c) rosette, and (d) sphere and their magnified surfaces. 1 and 2 represent the (104) facet and (rough) facet, respectively. Black arrows indicate the incorporated gel fibers. (e) C/Ca ratio of each point measured by EDS. (NS: $p > 0.05$, *$p < 0.01$, **$p < 0.001$.)

The crystals formed at the initial reaction time were observed with SEM to obtain further information on the origin of four shapes of $CaCO_3$ crystals. After 4 h, ACC nanoparticles were observed near the Ca^{2+} reservoir, and their diameter was ~142 nm. ACC nanoparticles were aggregated and gradually transformed into a sphere of ~5 μm (Figure 5a).

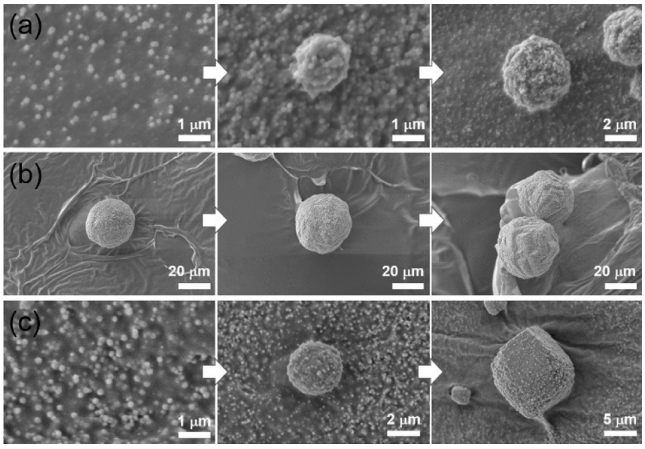

Figure 5. SEM micrographs of $CaCO_3$ formed after 4 h at (a) near Ca^{2+} reservoir, (b) Mid, and (c) near CO_3^{2-} reservoir under 0.2 M $CaCl_2$ and 0.2 M Na_2CO_3.

In the Mid position, no separated nanoparticle was observed; instead, aggregated spheres were found with a size of ~20 μm (Figure 5b). They developed into a cauliflower shape, and then the edges were developed on the surface, resulting in rosette crystals. It implies that the rosette originated from the sphere. On the other hand, a different crystallization process was observed near the CO_3^{2-} reservoir (Figure 5c). First, numerous ACC nanoparticles were formed. Then, some

https://doi.org/10.1021/acs.cgd.4c01159
Cryst. Growth Des. 2024, 24, 9994−10002

ACC was dissolved to supply the ion source to the seed point, resulting in a depletion rim around the seed.[38] Finally, the seed particles were grown to rhombohedron or otoconia crystals of ~5 μm.

To support the experimental observation, we developed a mathematical (reaction-diffusion) model containing the diffusion of the chemical species, a reversible reaction between reagents (Ca^{2+} and CO_3^{2-} ions) and intermediates, the effect of electrostatic stabilization by the excess of either Ca^{2+} or CO_3^{2-}, and the corresponding chemical equilibria. In this model, intermediates are considered nanoparticles, which have been observed in SEM analysis (Figure 5). The calculation successfully simulated precipitation phenomena (Figure 6).

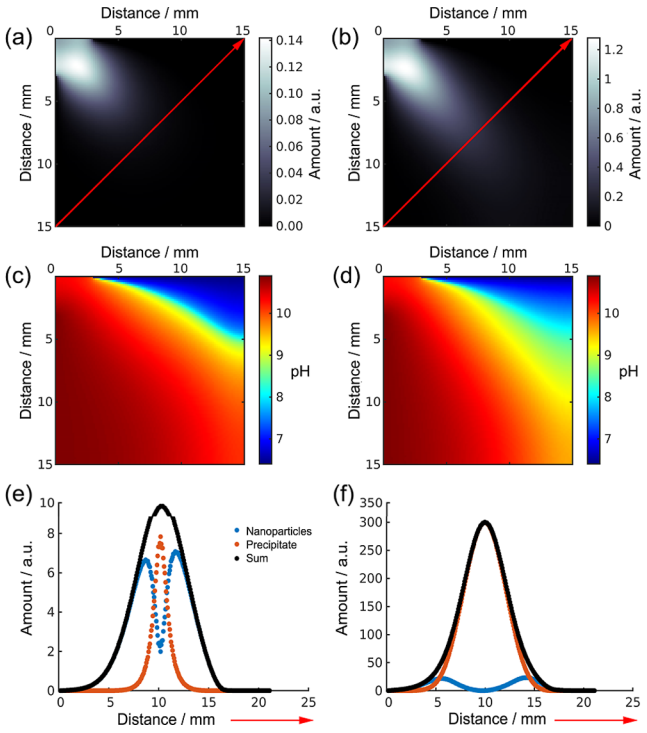

Figure 6. Simulation of crystallization in an orthogonal diffusion system at an early (left) and a late (right) stage. (a,b) Amount of products and (c,d) pH in a 2-dimensional cross-section of the hydrogel. (e,f) Amount of nanoparticles, precipitate, and sum of them as a function of diagonal distance marked as red arrows in (a,b).

The precipitation area gradually expanded along the diagonal direction between the Ca^{2+} and CO_3^{2-} reservoirs (Figure 6a,b). pH was the highest at the interface of the CO_3^{2-} reservoir, and it gradually decreased as it got close to the Ca^{2+} reservoir (Figure 6c). Noticeably, the pH was lowered in the area near the Ca^{2+} reservoir at the late stage (Figure 6d). While the formation of nanoparticles was dominant at the early stage in both the near Ca^{2+} and CO_3^{2-} reservoirs, precipitation was dominant between both reservoirs (Figure 6e). At the late stage, the amount of precipitate overwhelms the quantity of nanoparticles (Figure 6f). The simulation results align with the observed phenomenon after 4 h (Figure 5). Although the nanoparticles were dominant in both the near Ca^{2+} and the CO_3^{2-} reservoir, their amount was slightly lower in the near CO_3^{2-} than the near Ca^{2+} reservoir. The slight difference may result in the depletion of nanoparticles around the aggregate in the near CO_3^{2-} reservoir (Figure 5c). Nucleation and growth occur most rapidly at the Mid position, where the ratio of Ca^{2+} to CO_3^{2-} is close to 1:1. As the ratio deviates from 1:1, it favors the formation of nanoparticles. The crystallization of nanoparticles is influenced by the pH. Crystallization occurs more rapidly at higher pH. Hence, the depletion region is observed only near the CO_3^{2-} reservoir.

DISCUSSION

We noticed differences in surface texture depending on the form of $CaCO_3$ and speculated that different crystallization mechanisms may cause the differences. The sphere formed near the Ca^{2+} reservoir has a rough surface because of nanoparticle aggregation. At this position, crystallization occurs in relatively acidic environments due to the larger Ca^{2+} flux compared to the CO_3^{2-} flux, which has been confirmed by simulation results. In environments with a high ratio of calcium ions and low pH, the particle attachment mechanism is preferred because ACC particles formed kinetically can persist for an extended period, although they are thermodynamically unstable.[39] On the other hand, crystals such as otoconia formed near the CO_3^{2-} reservoir exhibit smooth and solid surface textures, indicating crystallization via an ion-by-ion mechanism. At this position, crystallization occurs in a relatively high pH environment where the CO_3^{2-} flux surpasses the Ca^{2+} flux. The precursor formed in the early stages of the reaction is dissolved and supplies ions to the nuclei, resulting in the growth of calcite. A depletion rim around the calcite crystals supports the dissolution−recrystallization processes.[40] Although the ratio of Ca^{2+} to CO_3^{2-} deviates significantly from 1:1, thermodynamically stable crystals with smooth surfaces are formed by transition through ion attachment in high pH environments.[41]

Our experimental setup inherently resulted in differences in the ion flux ratio at all positions due to the simultaneous supply of calcium and carbonate ions from perpendicular directions into the same hydrogel. The difference in flux between Ca^{2+} and CO_3^{2-} influences the initial conditions of the crystallization process and ultimately leads to the formation of different crystals. According to previous reports, the difference in the coordination number of Ca^{2+} and CO_3^{2-} ions is an essential factor influencing the crystallization process; a more significant number of Ca^{2+} ions can surround the CO_3^{2-} ions in contrast to the opposite case.[42,43] This means that ions aggregate more rapidly in solutions with an excess of Ca^{2+}, leading to the formation of nanoparticles. Indeed, it has been observed that nanoparticle formation is preferred under Ca^{2+} excess conditions compared to CO_3^{2-} excess solutions.[28]

In regions where Ca^{2+} flux is higher than CO_3^{2-} flux, despite being a nonstoichiometric condition, precursors quickly become supersaturated due to the abundant supply of Ca^{2+} flux, leading to the rapid formation of numerous ACC nanoparticles. Gebauer et al. have also proposed that ACC formed gradually at pH 9−10 is more stable, which aligns with the pH near the Ca^{2+} reservoir where crystallization occurs according to our simulation results.[44] As the stability of ACC precursors increases under less alkaline conditions, nanoparticles can persist for a more extended period. Subsequently, over time, ACC precursors spontaneously aggregate to form submicrometer-sized spherical aggregates through continuous particle attachment to the particle surfaces. This result is consistent with a previous report that an excess of Ca^{2+} ions ($[Ca^{2+}]/[CO_3^{2-}]$ = 5:1) slows down the process of particle formation and promotes the growth of spheroidal particles.[19]

https://doi.org/10.1021/acs.cgd.4c01159
Cryst. Growth Des. 2024, 24, 9994−10002

In contrast, in regions where the CO_3^{2-} flux exceeds the Ca^{2+} flux, crystallization occurs gradually as Ca^{2+} ions are supplied after a rapid supply of CO_3^{2-} ions. Over time, as the supply of Ca^{2+} ions accumulates, the degree of supersaturation gradually increases, reaching a threshold level where ACC precursors are formed. Some of the formed ACC nanoparticles develop into nuclei in a critical size, and, through Ostwald ripening, smaller ACC particles dissolve and recrystallize onto the critical nuclei, forming more matured crystals. Under Ca^{2+}-limited conditions, slow crystallization occurs due to low supersaturation, and distorted calcite, such as otoconia, is formed through selective growth of specific faces. Therefore, while the attachment of ACC precursors onto crystal faces is an essential mechanism for crystal growth, the growth via ion-by-ion attachment of single ions also occurs simultaneously.

On the other hand, in regions where Ca^{2+} and CO_3^{2-} flux are similar, the ratio of Ca^{2+} ions to CO_3^{2-} ions approaches stoichiometry. Under the stoichiometric condition, it has been reported that larger crystals are formed compared to nonstoichiometric conditions.[28] Indeed, in these regions, large crystals with sizes exceeding 50 μm are formed, and these crystals are differentiated into rosette and rhombohedral shapes due to slight differences in the flux of both ions. In locations where the ratio of Ca^{2+} flux is slightly higher, rosette crystals that resemble sphere shapes are formed. In contrast, in locations where the ratio of the CO_3^{2-} flux is slightly higher, rhombohedron shapes less distorted than otoconia are formed due to the selective growth of crystal surfaces.

The difference in these mechanisms is based on the assumption that amorphous precursors are formed through the aggregation of small ion clusters (prenucleation clusters) in the early stages of crystallization, and two types of precursors can be formed based on the local structure of ion clusters depending on pH.[44] Recent studies suggest that a dual mechanism involving particle attachment and ion-by-ion space filling should be considered in the formation of $CaCO_3$ minerals.[41] Through BET surface analysis, it has been confirmed that mature coral skeletons fill spaces on a micrometer scale comparable to those of geological aragonite single crystals.[41] It is argued that ion-by-ion attachment is essential to fill interstitial pores because amorphous particles alone cannot completely fill the space. Generally, crystals formed by particle attachment of amorphous precursors according to the nonclassical mechanism have rough surfaces and exhibit features such as porosity and defects. In contrast, crystals formed by ion-by-ion attachment according to the classical mechanism have smooth surfaces and exhibit classical features of crystal surface formation such as terrace, step, and kink.

CONCLUSIONS

The various calcite morphologies were observed in hydrogel media by introducing orthogonal diffusion. When two constituent ions were orthogonally diffused in a hydrogel, various environments with different ion fluxes and ratios were created due to slow diffusion. Therefore, it was possible to control the crystallization microenvironment precisely and systematically analyze the origin of the morphology transition. Our previous study demonstrated that various forms of $CaCO_3$ are controlled by the supply rate of single ions in a single diffusion system, and various calcite structural formation mechanisms were proposed based on differences in single ion flux. In this study, we aimed to overcome the limitations of single diffusion systems and investigate the process of controlling various forms of $CaCO_3$ in an orthogonal diffusion system of dual ions. Specifically, among the many parameters for controlling crystal morphology, it was found that the stoichiometry of ions or ion flux ratio plays a crucial role as the main factor.

AUTHOR INFORMATION

Corresponding Authors

István Lagzi − *Department of Physics, Institute of Physics and HU-REN-BME Condensed Matter Physics Research Group, Budapest University of Technology and Economics, Budapest 1111, Hungary;* orcid.org/0000-0002-2303-5965; Email: lagzi.istvan.laszlo@ttk.bme.hu

Sung Ho Yang − *Department of Chemistry Education, Korea National University of Education (KNUE), Cheongju 28173, Republic of Korea;* orcid.org/0000-0002-2744-8396; Email: sunghoyang@knue.ac.kr

Authors

Yu Seob Shin − *Department of Chemistry Education, Korea National University of Education (KNUE), Cheongju 28173, Republic of Korea*

Gábor Holló − *Department of Fundamental Microbiology, University of Lausanne, Lausanne 1015, Switzerland;* orcid.org/0000-0001-9920-4801

Complete contact information is available at: https://pubs.acs.org/10.1021/acs.cgd.4c01159

Author Contributions

⊥Y.S.S. and G.H. contributed equally.

Notes

The authors declare no competing financial interest.

ACKNOWLEDGMENTS

This work was supported by the Basic Science Research Program through the National Research Foundation of Korea (NRF) funded by the Ministry of Science and ICT (2019R1A2C1004247 and 2022R1A2C1005809), the National Research, Development and Innovation Office of Hungary (K146071), the HUN-REN Hungarian Research Network, the Ministry of Culture and Innovation, and the National Research, Development and Innovation Office under Grant No. TKP2021-EGA-02.

REFERENCES

(1) Zhou, Y.; Liu, K.; Zhang, H. Biomimetic Mineralization: from Microscopic to Macroscopic Materials and Their Biomedical Applications. *ACS Appl. Bio Mater.* **2023**, *6*, 3516−3531.

(2) Zhang, Y.; Ma, S.; Nie, J.; Liu, Z.; Chen, F.; Li, A.; Pei, D. Journey of Mineral Precursors in Bone Mineralization: Evolution and Inspiration for Biomimetic Design. *Small* **2024**, *20*, 2207951.

(3) Song, K.; Bang, J. H.; Chae, S. C.; Kim, J.; Lee, S. W. Phase and Morphology of Calcium Carbonate Precipitated by Rapid Mixing in the Absence of Additives. *RSC Adv.* **2022**, *12*, 19340−19349.

(4) Liendo, F.; Arduino, M.; Deorsola, F. A.; Bensaid, S. Factors Controlling and Influencing Polymorphism, Morphology and Size of Calcium Carbonate Synthesized through the Carbonation Route: A review. *Powder Technol.* **2022**, *398*, 117050.

(5) Ganot, P.; Tambutte, E.; Caminiti-Segonds, N.; Toullec, G.; Allemand, D.; Tambutte, S. Ubiquitous Macropinocytosis in Anthozoans. *eLife* **2020**, *9*, No. e50022.

(6) Boonrungsiman, S.; Gentleman, E.; Carzaniga, R.; Evans, N. D.; McComb, D. W.; Porter, A. E.; Stevens, M. M. The role of

Intracellular Calcium Phosphate in Osteoblast-Mediated Bone Apatite formation. *Proc. Natl. Acad. Sci. U.S.A.* **2012**, *109*, 14170−14175.
(7) Zeng, Y.; Cao, J.; Wang, Z.; Guo, J.; Zhou, Q.; Lu, J. Insights into the Confined Crystallization in Microfluidics of Amorphous Calcium Carbonate. *Cryst. Growth Des.* **2018**, *18*, 6538−6546.
(8) Kim, Y. Y.; Freeman, C. L.; Gong, X.; Levenstein, M. A.; Wang, Y.; Kulak, A.; Anduix-Canto, C.; Lee, P. A.; Li, S.; Chen, L.; et al. The Effect of Additives on the Early Stages of Growth of Calcite Single Crystals. *Angew. Chem., Int. Ed.* **2017**, *56*, 11885−11890.
(9) Kim, H.; Holló, G.; Heo, C. M.; Lagzi, I.; Lee, H.; Yang, S. H. Diffusion-Limited Growth of Calcium Phosphate for Macroscale Fabrication of Mineralized Gelatin Hydrogels. *Cryst. Growth Des.* **2024**, *24*, 8794−8802.
(10) Jung, J.; Yang, S. H. Diffusion-Controlled Crystallization of Fluorapatite Mesocrystals in a Hydrogel. *Cryst. Growth Des.* **2023**, *23*, 8753−8760.
(11) Cho, Y. S.; Moon, M.; Holló, G.; Lagzi, I.; Yang, S. H. Bioinspired Control of Calcium Phosphate Liesegang Patterns Using Anionic Polyelectrolytes. *Langmuir* **2022**, *38*, 2515−2524.
(12) Kim, H. L.; Shin, Y. S.; Yang, S. H. Effect of Poly(acrylic acid) on Crystallization of Calcium Carbonate in a Hydrogel. *CrystEngComm* **2022**, *24*, 1344−1351.
(13) Shin, Y. S.; Jo, M.; Cho, Y. S.; Yang, S. H. Diffusion-Controlled Crystallization of Calcium Phosphate in a Hydrogel Toward a Homogeneous Octacalcium Phosphate/Agarose Composite. *ACS Omega* **2022**, *7*, 1173−1185.
(14) Jo, M.; Cho, Y. S.; Holló, G.; Choi, J.-M.; Lagzi, I.; Yang, S. H. Spatiotemporal and Microscopic Analyses of Asymmetric Liesegang Bands: Diffusion-Limited Crystallization of Calcium Phosphate in a Hydrogel. *Cryst. Growth Des.* **2021**, *21*, 6119−6128.
(15) Jo, M. K.; Oh, Y.; Kim, H. J.; Kim, H. L.; Yang, S. H. Diffusion-Controlled Crystallization of Calcium Carbonate in a Hydrogel. *Cryst. Growth Des.* **2020**, *20*, 560−567.
(16) Palin, D.; Style, R. W.; Zlopaša, J.; Petrozzini, J. J.; Pfeifer, M. A.; Jonkers, H. M.; Dufresne, E. R.; Estroff, L. A. Forming Anisotropic Crystal Composites: Assessing the Mechanical Translation of Gel Network Anisotropy to Calcite Crystal Form. *J. Am. Chem. Soc.* **2021**, *143*, 3439−3447.
(17) Bielak, K.; Różycka, M. O.; Zoglowek, A.; Ozyhar, A.; Dobryszycki, P. Counter-Diffusion System as an in Vitro Model in the Investigation of Proteins Involved in the Formation of Calcium Carbonate Biominerals. *Cryst. Growth Des.* **2021**, *21*, 1389−1400.
(18) Asenath-Smith, E.; Li, H.; Keene, E. C.; Seh, Z. W.; Estroff, L. A. Crystal growth of calcium carbonate in hydrogels as a model of biomineralization. *Adv. Funct. Mater.* **2012**, *22*, 2891−2914.
(19) Bahrom, H.; Goncharenko, A. A.; Fatkhutdinova, L. I.; Peltek, O. O.; Muslimov, A. R.; Koval, O. Y.; Eliseev, I. E.; Manchev, A.; Gorin, D.; Shishkin, I. I.; et al. Controllable Synthesis of Calcium Carbonate with Different Geometry: Comprehensive Analysis of Particle Formation, Cellular Uptake, and Biocompatibility. *ACS Sustain. Chem. Eng.* **2019**, *7*, 19142−19156.
(20) Svenskaya, Y. I.; Fattah, H.; Inozemtseva, O. A.; Ivanova, A. G.; Shtykov, S. N.; Gorin, D. A.; Parakhonskiy, B. V. Key Parameters for Size-and Shape-Controlled Synthesis of Vaterite Particles. *Cryst. Growth Des.* **2018**, *18*, 331−337.
(21) Tai, C. Y.; Chen, C. K. Particle Morphology, Habit, and Size Control of $CaCO_3$ Using Reverse Microemulsion Technique. *Chem. Eng. Sci.* **2008**, *63*, 3632−3642.
(22) Castillo Alvarez, C. C.; Penkman, K.; Kröger, R.; Finch, A. A.; Clog, M.; Brasier, A.; Still, J.; Allison, N. Insights into the Response of Coral Biomineralisation to Environmental Change from Aragonite Precipitations in vitro. *Geochim. Cosmochim. Acta* **2024**, *364*, 184−194.
(23) Sand, K. K.; Tobler, D. J.; Dobberschütz, S.; Larsen, K. K.; Makovicky, E.; Andersson, M. P.; Wolthers, M.; Stipp, S. L. S. Calcite Growth Kinetics: Dependence on Saturation Index, Ca^{2+}:CO_3^{2-} Activity Ratio, and Surface Atomic Structure. *Cryst. Growth Des.* **2016**, *16*, 3602−3612.
(24) Wolthers, M.; Nehrke, G.; Gustafsson, J. P.; Van Cappellen, P. Calcite Growth Kinetics: Modeling the Effect of Solution Stoichiometry. *Geochim. Cosmochim. Acta* **2012**, *77*, 121−134.
(25) Ruiz-Agudo, E.; Putnis, C. V.; Rodriguez-Navarro, C.; Putnis, A. Effect of pH on calcite growth at constant ratio and supersaturation. *Geochim. Cosmochim. Acta* **2011**, *75*, 284−296.
(26) Larsen, K.; Bechgaard, K.; Stipp, S. L. S. The Effect of the Ca^{2+} to CO_3^{2-} Activity Ratio on Spiral Growth at the Calcite $\{10\bar{1}4\}$ Surface. *Geochim. Cosmochim. Acta* **2010**, *74*, 2099−2109.
(27) He, H.; Chen, L.; Wang, Z.; Zhang, L.; Ge, T.; Xiang, X.; Wang, S.; Huang, Y.; Li, S. Screening the Ion Compositions on Crystal Morphology Transitions by a Microfluidic Chip with a Well-Defined Concentration Gradient. *Cryst. Growth Des.* **2020**, *20*, 6877−6887.
(28) Seepma, S. Y.; Ruiz-Hernandez, S. E.; Nehrke, G.; Soetaert, K.; Philipse, A. P.; Kuipers, B. W.; Wolthers, M. Controlling $CaCO_3$ Particle Size with $\{Ca^{2+}\}$:$\{CO_3^{2-}\}$ Ratios in Aqueous Environments. *Cryst. Growth Des.* **2021**, *21*, 1576−1590.
(29) Perdikouri, C.; Putnis, C. V.; Kasioptas, A.; Putnis, A. An Atomic Force Microscopy Study of the Growth of a Calcite Surface as a Function of Calcium/Total Carbonate Concentration Ratio in Solution at Constant Supersaturation. *Cryst. Growth Des.* **2009**, *9*, 4344−4350.
(30) Luo, X.; Song, X.; Cao, Y.; Song, L.; Bu, X. Investigation of Calcium Carbonate Synthesized by Steamed Ammonia Liquid Waste without Use of Additives. *RSC Adv.* **2020**, *10*, 7976−7986.
(31) Price, S. L. Progress in Understanding Crystallisation: a Personal Perspective. *Faraday Discuss.* **2022**, *235*, 569−581.
(32) Farkas, S.; Fonyi, M. S.; Holló, G.; Német, N.; Valletti, N.; Kukovecz, A.; Schuszter, G.; Rossi, F.; Lagzi, I. Periodic Precipitation of Zeolitic Imidazolate Frameworks in a Gelled Medium. *J. Phys. Chem. C* **2022**, *126*, 9580−9586.
(33) Farkas, S.; Holló, G.; Schuszter, G.; Deák, Á.; Janovák, L.; Hornok, V.; Itatani, M.; Nabika, H.; Horváth, D.; Tóth, Á.; Lagzi, I. Reaction−Diffusion Assisted Synthesis of Gold Nanoparticles: Route from the Spherical Nano-Sized Particles to Micrometer-Sized Plates. *J. Phys. Chem. C* **2021**, *125*, 26116−26124.
(34) Park, J. H.; Paczesny, J.; Kim, N.; Grzybowski, B. A. Shaping Microcrystals of Metal-Organic Frameworks by Reaction-Diffusion. *Angew. Chem., Int. Ed.* **2020**, *59*, 10301−10305.
(35) Saliba, D.; Ammar, M.; Rammal, M.; Al-Ghoul, M.; Hmadeh, M. Crystal Growth of ZIF-8, ZIF-67, and Their Mixed-Metal Derivatives. *J. Am. Chem. Soc.* **2018**, *140*, 1812−1823.
(36) Patel, A. R.; Venkateswara Rao, A. Crystal Growth in Gel Media. *Bull. Mater. Sci.* **1982**, *4*, 527−548.
(37) Jiang, F.; Xu, X. W.; Chen, F. Q.; Weng, H. F.; Chen, J.; Ru, Y.; Xiao, Q.; Xiao, A. F. Extraction, Modification and Biomedical Application of Agarose Hydrogels: a Review. *Mar. Drugs* **2023**, *21*, 299.
(38) Yang, S. H.; Choi, I. S. Rosette-Shaped Calcite Structures at Surfaces: Mechanistic Implications for $CaCO_3$ Crystallization. *Chem.—Asian J.* **2010**, *5*, 1586−1593.
(39) Schoeppler, V.; Stier, D.; Best, R. J.; Song, C.; Turner, J.; Savitzky, B. H.; Ophus, C.; Marcus, M. A.; Zhao, S.; Bustillo, K.; et al. Crystallization by Amorphous Particle Attachment: on the Evolution of Texture. *Adv. Mater.* **2021**, *33*, 2101358.
(40) Liu, Z.; Zhang, Z.; Wang, Z.; Jin, B.; Li, D.; Tao, J.; Tang, R.; De Yoreo, J. J. Shape-Preserving Amorphous-to-Crystalline Transformation of $CaCO_3$ Revealed by In Situ TEM. *Proc. Natl. Acad. Sci. U.S.A.* **2020**, *117*, 3397−3404.
(41) Sun, C. Y.; Stifler, C. A.; Chopdekar, R. V.; Schmidt, C. A.; Parida, G.; Schoeppler, V.; Fordyce, B. I.; Brau, J. H.; Mass, T.; Tambutté, S.; et al. From Particle Attachment to Space-Filling Coral Skeletons. *Proc. Natl. Acad. Sci. U.S.A.* **2020**, *117*, 30159−30170.
(42) Demichelis, R.; Raiteri, P.; Gale, J. D.; Quigley, D.; Gebauer, D. Stable Prenucleation Mineral Clusters are Liquid-like Ionic Polymers. *Nat. Commun.* **2011**, *2*, 590.
(43) Smeets, P. J. M.; Cho, K. R.; Kempen, R. G. E.; Sommerdijk, N. A. J. M.; De Yoreo, J. J. In Situ TEM Shows Ion Binding is Key to

https://doi.org/10.1021/acs.cgd.4c01159
Cryst. Growth Des. 2024, 24, 9994−10002

Directing $CaCO_3$ Nucleation in a Biomimetic Matrix. *Nat. Mater.* **2015**, *14*, 394−399.
(44) Gebauer, D.; Gunawidjaja, P. N.; Ko, J. Y. P.; Bacsik, Z.; Aziz, B.; Liu, L.; Hu, Y.; Bergström, L.; Tai, C.; Sham, T.; et al. Proto-Calcite and Proto-Vaterite in Amorphous Calcium Carbonates. *Angew. Chem., Int. Ed.* **2010**, *49*, 8889−8891.

https://doi.org/10.1021/acs.cgd.4c01159
Cryst. Growth Des. 2024, 24, 9994−10002